Mechanical Systems and Signal Processing 127 (2019) 513–530

Contents lists available at ScienceDirect

Mechanical Systems and Signal Processing

journal homepage: www.elsevier.com/locate/ymssp

Robust cascade control of a deployable cable-driven robot

S.A. Khalilpour [a], R. Khorrambakht [a], H.D. Taghirad [a,*], Philippe Cardou [b]

[a] Advanced Robotics and Automated Systems (ARAS), Industrial Control Center of Excellence (ICCE), Faculty of Electrical and Computer Engineering, K.N. Toosi University of Technology, Iran
[b] Department of Mechanical Engineering, Robotics Laboratory, Laval University, Quebec City, QC G1V 0A6, Canada

ARTICLE INFO

Article history:
Received 23 December 2018
Received in revised form 26 February 2019
Accepted 6 March 2019

Keywords:
Cable-driven parallel manipulator
Robust control
Sliding mode control
Force sensor
Cascade topology

ABSTRACT

In this paper, we derive the dynamic formulation of a deployable cable-driven robot that considers models of the actuator and power transmission systems, and we investigate the challenges of structural uncertainty. To accommodate the inherent uncertainty of the system, we propose a proper control topology based on a cascade structure. The inner loop of the structure controls the cable forces, and the outer loop tracks the precise position of the robot's end-effector. For the design of the outer loop controller, we propose a robust sliding mode controller with a stability analysis that is based on the Lyapunov direct method. The main contribution of this paper is to analyze the stability of the system as a whole considering both the inner and outer loop controllers. Finally, in order to illustrate the performance of the proposed controller, we present the results of an experiment on a deployable suspended cable-driven robot, which shows the effectiveness of the proposed controller in the presence of the inherent uncertainties of the system.

© 2019 Elsevier Ltd. All rights reserved.

1. Introduction

A cable-driven parallel manipulator (CDPM) is a robots whose end-effector pose is controlled by winding and unwinding independent cables connecting the end effector to the fixed base [1]. These robots have several advantages, including a large workspace, high speed and acceleration capabilities, and a simple mechanical structure. The idea of cable-driven robots that are quick and easy to deploy was first proposed in [2–4], which targetted their applications in rescue missions. Due to the aforementioned advantages, this class of robots are suited to many rescue-mission scenarios. [5]. Other potential applications include agriculture and automated farming [2].

For deployable suspended cable-driven robots (DSCRs), the kinematic parameters are not accurately measured, and as a result characteristic parameters of the robot model are perturbed. This in turn, introduces many challenges in terms of controller design and meeting the required performance [3,6–10]. Despite of these inaccuracies and because of their simplicity, for the applications where fine precision is not required, these robots have proven to be useful. In fact, a family of cable-driven robots known as Spider-cams are commonly used for video capturing applications at sport fields. As shown in Fig. 1, ARAS-CAM robot as an example of a deployable suspended cable-driven robot (DSCR), is also specially designed for video capturing applications. The simplicity of installation as the main characteristics of DSCR makes it extremely suitable in the field of video capturing applications.

---

[*] Corresponding author at: Advanced Robotics and Automated Systems (ARAS), Industrial Control Center of Excellence (ICCE), Faculty of Electrical and Computer Engineering, K.N. Toosi University of Technology, P.O. Box 16315-1355, Tehran, Iran.

E-mail addresses: khalilpour@ee.kntu.ac.ir (S.A. Khalilpour), taghirad@kntu.ac.ir (H.D. Taghirad), pcardou@gmc.ulaval.ca (P. Cardou).

https://doi.org/10.1016/j.ymssp.2019.03.010
0888-3270/© 2019 Elsevier Ltd. All rights reserved.

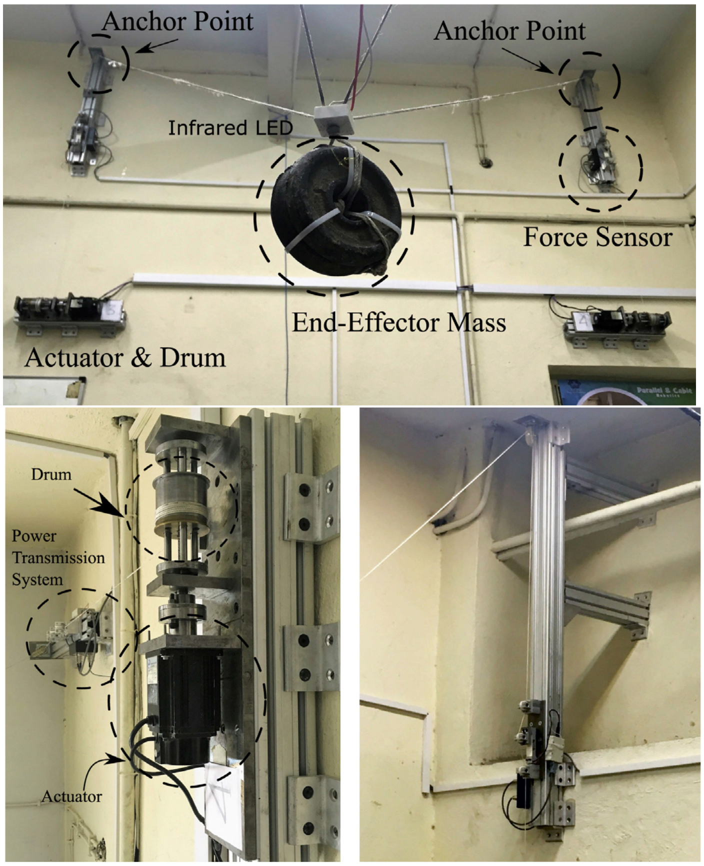

Fig. 1. Prototype of a deployable suspended cable-driven robot called ARAS-CAM.

In addition to kinematic uncertainty, DSCRs suffer from several dynamic uncertainties as well. These dynamic uncertainties have different origins. They are related to robot geometry and structural uncertainty in addition to actuators and power transmission systems, none of which can be accurately modeled. Both structural and non-structural dynamic uncertainties have a profound effect on the robot trajectory tracking performance. Hence, a robust control structure is needed to minimize the effect of these sources of errors.

Several successful robust controllers have been proposed in the literature for various applications of CDPMs. A category of such controllers, called sliding mode controllers (SMCs), are known to be effective in many applications in the presence of modeling uncertainty [11,12]. In this paper, we propose a robust sliding mode controller in order to overcome the problems of kinematic and dynamic uncertainties. We implement this method via a cascade structure, in which the inner loop is designed to control the cable forces and the outer loop is designed to control the end-effector position. We also achieve simultaneous tracking of the desired end-effector position and cable forces by defining a new sliding surface, which is composed of the position and force errors. A robust force tracking system makes it possible to mitigate the negative effects of the complex, non-linear, high-order dynamics (like friction) that are often found in the actuators and power transmission systems.

In the field of robotics, most of the common control systems are based on a cascade structure in which the inner controller is assumed to be a fast high-bandwidth controller, and the outer controller (a user-specified control loop) is responsible for the robot's main objective: trajectory tracking. The effectiveness of such an approach depends on the assumption that the inner loop controller is fast enough, and thus that its dynamics may be ignored. In practice, such an assumption generally cannot be made. Therefore, we analyze the whole structure of the cascade controller and investigate the effect of selected structures and coefficients for the inner loop controller. Here, the inner loop controller is designed to mitigate the adverse effects of dynamic uncertainty (of the actuators and power transmission systems, i.e. pulleys) on force tracking. These effects are more notable when the cables are directly driven by the motors. To overcome the uncertainties caused by an inaccurate kinematic structure, a robust controller based on the well-known dynamic sliding mode method is designed [13–16].

The main contribution of this paper is to consider an inner-loop force control structure and to design and analyze the overall system stability using Lyapunov's direct method. In such a control system, the end-effector position can be derived by using either forward kinematics relations [17], or an accurate position sensor [18,19]. In either cases, The measured position is then compared to the desired location of the end-effector. Next, the inner-loop control command—namely the desired cable tension—is calculated. Finally, the cable force error is computed by comparing this command to cable forces directly measured by the force sensors. Following that, using this error, control commands are computed and sent to the motors.

One of the most difficult aspects of implementing the cascade methods is selecting a appropriate gain for the inner loop controller. A low gain controller cannot provide proper force tracking, but the presence of measurement noise in the force sensors may prohibit high gains from being assigned. That is why we seek to investigate the issue of proper inner-loop gain selection for a deployable cable-driven parallel robot.

The remainder of this paper is organized as follows. First, we present the kinematic formulation of a DSCR and its Jacobian analysis. Next, we formulate the actuators and power transmission dynamics and present the dynamic model of the cable-driven robot as a whole. Then, we introduce the proposed robust control law and analyze the robust stability of the closed-loop system. Finally, we present the results of our experiments, which illustrate the proposed controller's ability to achieve a suitable level of performance.

2. Kinematics formulation

The kinematic modeling of DSCR is investigated in this section. In the first step, we derive the kinematic equations. Next, through differentiation, the Jacobian matrix is also constructed. Fig. 2 illustrates a DSCR constrained by four cables, all of which are attached to a single point on the end-effector. For driving the equations, the end-effector is treated as a lumped mass at the intersection of the cables. Following this assumption, the loop closure method for this manipulator is applied as shown in Fig. 2 and given as follows.

$$\vec{\boldsymbol{L}_i} = \vec{\boldsymbol{P}} - \overrightarrow{\boldsymbol{P}_{A_i}}, \quad i = 1, \dots, 4. \tag{1}$$

In what follows, the inverse kinematics relations and the Jacobian matrix of the robot are derived.

2.1. Inverse kinematics solution

Writing the loop closer equations algebraically leads to

$$l_i^2 = \left(\boldsymbol{P} - \boldsymbol{P}_{A_i}\right)^T \left(\boldsymbol{P} - \boldsymbol{P}_{A_i}\right), \tag{2}$$

in which l_i is the length of i'th cable. Decomposing the equations into their component-wise forms leads to:

$$l_i = \sqrt{(x - x_i)^2 + (y - y_i)^2 + (z - z_i)^2}, \tag{3}$$

in which x, y, z and x_i, y_i, z_i respectively denote the position of end-effector and i'th cables attachment points.

2.2. Forward kinematics solution

Having just three of the four equations of (3) for $i = 1, 2, \dots, 4$, the end-effector position can be directly calculated. For instance, if cable 1–3 equations are chosen, the solution of the DSCR forward kinematic would be written as

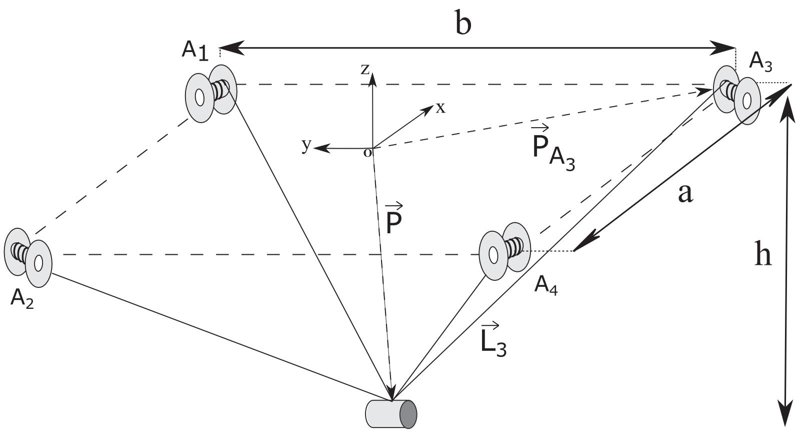

Fig. 2. Kinematic schematics of a deployable suspended cable-driven robot.

$$\begin{aligned} x &= \tfrac{1}{2a}\left(l_2^2 - l_3^2\right), \quad y = \tfrac{1}{2b}\left(l_1^2 - l_2^2\right), \\ z &= h \pm \sqrt{l_1^2 - \left(x + \tfrac{a}{2}\right) - \left(y + \tfrac{b}{2}\right)}, \end{aligned} \tag{4}$$

For the z component there are two solutions. However, based on the physics of the robot, the negative solution is correct.

2.3. Jacobian matrix

Holding an integral role at kinematic analysis of the robot, the jacobian matrix provides a map between the joint and work spaces variables. Moreover, the Jacobian matrix relates the actuator torques to the forces represented in the workspace [20]. On the other hand, singularity analysis can also be carried out through the studying of the Jacobian matrix's characteristics at different configurations. For the robot under study, the jacobian matrix is derived as follows. Let $\boldsymbol{l}$ denote the vector represented in the joint coordinates and comprised of the cables' lengths and $\mathbf{x}$, denote the end-effector's motion vector. Thus, the kinematic equations could be derived as $\boldsymbol{f}(\boldsymbol{l}, \mathbf{x}) = 0$ which is an implicit function of vectors $\mathbf{x}$ and $\boldsymbol{l}$. Next, using the $\boldsymbol{f}(\boldsymbol{l}, \mathbf{x})$, the relation between joint and work space velocities, $\dot{\boldsymbol{l}}$ and $\dot{\mathbf{x}}$, can be derived by calculating the derivatives as follows:

$$\boldsymbol{J}_x \dot{\mathbf{x}} = \boldsymbol{J}_l \dot{\boldsymbol{l}}, \tag{5}$$

$$\boldsymbol{J}_x = +\frac{\partial \boldsymbol{f}}{\partial \mathbf{x}}, \quad \boldsymbol{J}_l = -\frac{\partial \boldsymbol{f}}{\partial \boldsymbol{l}}. \tag{6}$$

Hence, the Jacobian matrix can be derived as follows:

$$\dot{\boldsymbol{l}} = \boldsymbol{J}\dot{\mathbf{x}}, \tag{7}$$

$$\boldsymbol{J} = \boldsymbol{J}_L^{-1}\boldsymbol{J}_x. \tag{8}$$

In the case of the robot shown in Fig. 2, the Jacobian matrix is derived by performing such calculations as follows:

$$\boldsymbol{J} = \begin{bmatrix} \frac{(x-x_1)}{l_1} & \frac{(y-y_1)}{l_1} & \frac{(z-z_1)}{l_1} \\ \frac{(x-x_2)}{l_2} & \frac{(y-y_2)}{l_2} & \frac{(z-z_2)}{l_2} \\ \frac{(x-x_3)}{l_3} & \frac{(y-y_3)}{l_3} & \frac{(z-z_3)}{l_3} \\ \frac{(x-x_4)}{l_4} & \frac{(y-y_4)}{l_4} & \frac{(z-z_4)}{l_4} \end{bmatrix}. \tag{9}$$

3. Robot dynamic model

In some references like [21–23], cable flexibility effects have been investigated in detail and a complex model for the robot's dynamics has been presented. In these researches, the dimensions are so large that the effects of cable stiffness can not be neglected. On the other hand the mass of a lenghthy cable leads to sagging effects. However in our project, due to short length and high modulus of elasticity of the employed cables, the aforementioned effects are ignored. Following this, the dynamic model of a DSCR may be written in the general form as

$$\boldsymbol{M}(\mathbf{x})\ddot{\mathbf{x}} + \boldsymbol{C}(\mathbf{x}, \dot{\mathbf{x}})\dot{\mathbf{x}} + \boldsymbol{G} = \boldsymbol{F} = -\boldsymbol{J}^T\boldsymbol{\tau}, \tag{10}$$

where $\boldsymbol{M}, \boldsymbol{C}$, and $\boldsymbol{G}$ respectively denote the mass matrix, Coriolis and centripetal matrix, and gravity vector. Vectors $\mathbf{x}$ and $\boldsymbol{F}$ respectively denote the generalized coordinates of the end-effector position and the Cartesian wrench applied to it. Finally, $\boldsymbol{J}$ denotes the Jacobian matrix of the robot, and $\boldsymbol{\tau}$ is cable forces vector. In the case of ARAS-CAM in which all of the cables are attached to the end-effector at one point, the kinetic energy E_T of the moving platform can be computed as $E_T = \frac{1}{2}\dot{\mathbf{x}}^T m \boldsymbol{I}\dot{\mathbf{x}}$ in which m stands for end-effector mass and $\boldsymbol{I}$ indicates a 3×3 identity matrix. The potential energy E_U of the moving platform can be also calculated as $E_U = mgh$ where g stands for gravity and h introduces relative height. Using calculated kinematic and potential energy, Lagrange function can be written as $E_L = E_T - E_U$. Then, using Lagrange equation $\frac{d}{dt}\left(\frac{\partial E_L}{\partial \dot{\mathbf{x}}}\right) - \frac{\partial E_L}{\partial \mathbf{x}} = -\boldsymbol{J}^T\boldsymbol{\tau}$ and considering the Eq. (10), we can derive the value of $\boldsymbol{M}, \boldsymbol{C}$ and $\boldsymbol{G}$ for the ARAS-CAM. The dynamics of actuators and power transmission systems shown in Fig. 3 are also represented by

$$\boldsymbol{I}_M\ddot{\boldsymbol{\theta}}_M + \boldsymbol{D}_M\dot{\boldsymbol{\theta}}_M - r_M\boldsymbol{\tau}_{P_1} = r_M\boldsymbol{u}. \tag{11}$$

For the power transmission system, we have

$$\boldsymbol{I}_{P_i}\ddot{\boldsymbol{\theta}}_{P_i} + \boldsymbol{D}_{P_i}\dot{\boldsymbol{\theta}}_{P_i} - r_{P_i}\boldsymbol{\tau}_{P_{i+1}} = -r_{P_i}\boldsymbol{\tau}_{P_i}, \quad i = 1 : n-1, \tag{12}$$

and for the last pulley, we have

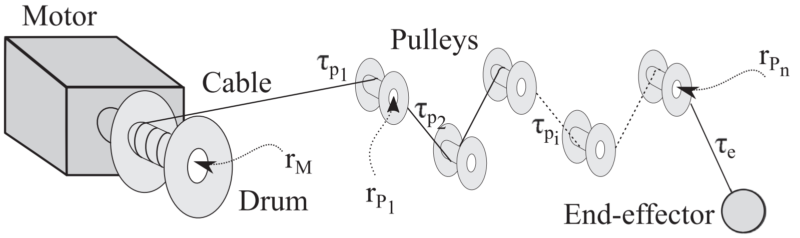

Fig. 3. Schematic of the power transmission systems.

$$\boldsymbol{I}_{P_n}\ddot{\boldsymbol{\theta}}_{P_n} + \boldsymbol{D}_{P_n}\dot{\boldsymbol{\theta}}_{P_n} - r_{P_n}\boldsymbol{\tau} = -r_{P_n}\boldsymbol{\tau}_{P_n}. \tag{13}$$

In which n denotes the number of pulleys, $\boldsymbol{\theta}_M, \boldsymbol{\theta}_{P_i}$ denote the angle vectors of the drum and i^{th} pulley, $\boldsymbol{I}_m, \boldsymbol{I}_{P_i}$ denote the inertia matrix of the drum and i^{th} pulley, $\boldsymbol{D}_M, \boldsymbol{D}_{P_i}$ denote the viscous friction matrix of the drum and i^{th} pulley, r_M, r_{P_i} denote the radius of the drum and pulley, $\boldsymbol{\tau}$ denotes the cable tension applied to the end-effector, $\boldsymbol{\tau}_{P_i}$ denotes the cable tension vector of the ith pulley, and $\boldsymbol{u}$ denotes the motor force vector.

We differentiate and use the manipulator Jacobian $\dot{\boldsymbol{l}} = \boldsymbol{J}\dot{\mathbf{x}}$ to reach

$$\dot{\boldsymbol{\theta}}_M = r_M^{-1}\dot{\boldsymbol{l}} = r_M^{-1}\boldsymbol{J}\dot{\mathbf{x}}, \quad \ddot{\boldsymbol{\theta}}_M = r_M^{-1}\boldsymbol{J}\ddot{\mathbf{x}} + r_M^{-1}\dot{\boldsymbol{J}}\dot{\mathbf{x}}, \tag{14}$$

$$\dot{\boldsymbol{\theta}}_{P_i} = r_{P_i}^{-1}\dot{\boldsymbol{l}} = r_{P_i}^{-1}\boldsymbol{J}\dot{\mathbf{x}}, \quad \ddot{\boldsymbol{\theta}}_{P_i} = r_{P_i}^{-1}\boldsymbol{J}\ddot{\mathbf{x}} + r_{P_i}^{-1}\dot{\boldsymbol{J}}\dot{\mathbf{x}}. \tag{15}$$

After manipulating the above equations, we reach to:

$$\boldsymbol{M}_T\ddot{\mathbf{x}} + \boldsymbol{C}_T\dot{\mathbf{x}} + \boldsymbol{G} = \boldsymbol{J}^T\boldsymbol{u}, \tag{16}$$

in which

$$\boldsymbol{M}_T = M + M_{PTS}, \qquad \boldsymbol{C}_T = \boldsymbol{C} + \boldsymbol{C}_{PTS}, \tag{17}$$

$$\boldsymbol{M}_{PTS} = r_M^{-2}\boldsymbol{J}^T\boldsymbol{I}_M\boldsymbol{J} + \sum_{i=1}^{n} r_{P_i}^{-2}\boldsymbol{J}^T\boldsymbol{I}_{P_i}\boldsymbol{J}, \tag{18}$$

$$\boldsymbol{C}_{PTS} = r_M^{-2}\boldsymbol{J}\boldsymbol{I}_M\dot{\boldsymbol{J}} + r_M^{-2}\boldsymbol{J}^T\boldsymbol{D}_M\boldsymbol{J} + \sum_{i=1}^{n} r_{P_i}^{-2}\boldsymbol{J}\boldsymbol{I}_{P_i}\dot{\boldsymbol{J}} + r_{P_i}^{-2}\boldsymbol{J}^T\boldsymbol{D}_{P_i}\boldsymbol{J}. \tag{19}$$

Eq. (16) represents the robot's dynamics as a whole, including consideration of the actuator and pulley dynamics.

4. Sliding surface definition

In this section, we use the position and force sensory data and desired trajectory as the basis for our proposal of the following sliding surfaces for robust control of the robot:

$$\boldsymbol{s}_r = \dot{\mathbf{x}} - \dot{\mathbf{x}}_r. \tag{20}$$

In the above equation, $\mathbf{x}_r$ is defined as a nominal reference for motion control, and is designed as

$$\dot{\mathbf{x}}_r = \dot{\mathbf{x}}_d - \boldsymbol{\Lambda}\tilde{\mathbf{x}} - \gamma\sigma, \tag{21}$$

in which $\dot{\mathbf{x}}_d$ is the desired velocity of the end-effector, and $\tilde{\mathbf{x}} = \mathbf{x} - \mathbf{x}_d, \gamma \in \boldsymbol{R}^{n\times n}$. Furthermore, $\boldsymbol{\Lambda} = diag(\Lambda_1, \Lambda_2, \cdots, \Lambda_n)$ is a symmetric positive definite diagonal matrix, and n denotes the robot's degrees of freedom.

In the above equation, $\dot{\sigma}$ is defined as

$$\dot{\sigma} = \hat{\boldsymbol{J}}^T\boldsymbol{\tau}_I - \hat{\boldsymbol{J}}^T\boldsymbol{\tau}, \tag{22}$$

in which $\boldsymbol{\tau}$ stands for the cable forces measured by the force sensors, and $\boldsymbol{\tau}_I$ is the desired tension force in the cables. This desired force should be positive to guarantee cable tensions in all configurations, and is stated as

$$-\hat{\boldsymbol{J}}^T\boldsymbol{\tau}_I = \boldsymbol{F}_I = \hat{\boldsymbol{M}}\ddot{\mathbf{x}}_I + \hat{\boldsymbol{C}}\dot{\mathbf{x}}_I + \hat{\boldsymbol{G}} - \boldsymbol{K}_I sgn(\boldsymbol{s}_x). \tag{23}$$

In the above equation, $\hat{\boldsymbol{M}}$, $\hat{\boldsymbol{C}}$, and $\hat{\boldsymbol{G}}$ respectively denote the approximate mass matrix, Coriolis term, and gravity vector, and function $sgn(\cdot)$ stands for the input wise discontinuous signum function. Also, $\dot{\mathbf{x}}_I$ is represented as

$$\dot{\mathbf{x}}_l = \dot{\mathbf{x}}_d - \Lambda\tilde{\mathbf{x}}. \tag{24}$$

Now, consider a second sliding surface as

$$\boldsymbol{s}_x = \dot{\tilde{\mathbf{x}}} + \Lambda\tilde{\mathbf{x}}. \tag{25}$$

Using the definition of $\boldsymbol{s}_x$, one can rewrite Eq. (22) as

$$\dot{\sigma} = \boldsymbol{M}\dot{\boldsymbol{s}}_x + \boldsymbol{C}\boldsymbol{s}_x + \boldsymbol{K}_l sgn(\boldsymbol{s}_x) + \rho_x, \tag{26}$$

where ρ_x is related to system uncertainty and can be encapsulated as

$$\rho_x = -\left(\tilde{\boldsymbol{M}}\ddot{\mathbf{x}}_l + \tilde{\boldsymbol{C}}\dot{\mathbf{x}}_l + \tilde{\boldsymbol{G}} + \tilde{\boldsymbol{J}}^T\boldsymbol{\tau}\right), \tag{27}$$

in which $\tilde{\boldsymbol{J}} = \hat{\boldsymbol{J}} - \boldsymbol{J}, \tilde{\boldsymbol{M}} = \hat{\boldsymbol{M}} - \boldsymbol{M}$, $\tilde{\boldsymbol{C}} = \hat{\boldsymbol{C}} - \boldsymbol{C}$, and $\tilde{\boldsymbol{G}} = \hat{\boldsymbol{G}} - \boldsymbol{G}$.

Some important properties of the derived dynamics equations are given as follows, which will be used in the stability analysis of the overall closed-loop system.

Property 1. The matrix $\boldsymbol{M}(\mathbf{x})$ is symmetric, positive definite, and upper and lower bounded for all $\mathbf{x}$, [24], as follows

$$\lambda_m < ||\boldsymbol{M}(\mathbf{x})|| < \lambda_M, \tag{28}$$

in which λ_m and λ_M respectively denote the minimum and maximum eigenvalues of the matrix $\boldsymbol{M}$.

Property 2. The $C(x,\dot{x})$ matrix and the time derivative of inertia matrix $M(x)$ satisfy

$$\dot{\mathbf{x}}^T\left[\frac{1}{2}\dot{M}(\mathbf{x}) - C(\mathbf{x},\dot{\mathbf{x}})\right]\dot{\mathbf{x}} = 0, \tag{29}$$

which reveals that the matrix $\dot{\boldsymbol{M}}(\mathbf{x}) - 2\boldsymbol{C}(\mathbf{x},\dot{\mathbf{x}})$ is skew-symmetric.

Property 3. The upper bounds of the Coriolis and centrifugal matrices are functions of $\dot{\mathbf{x}}$, as follows:

$$||\boldsymbol{C}(\mathbf{x},\dot{\mathbf{x}})|| < \zeta_c||\boldsymbol{s}_r||. \tag{30}$$

Property 4. The upper bound of the gravity matrix is

$$||\boldsymbol{G}(\mathbf{x})|| < \zeta_g. \tag{31}$$

5. The proposed control law

Fig. 4 shows the proposed control topology. The proposed control law is formulated by

$$\boldsymbol{u} = -\boldsymbol{K}_P(\boldsymbol{\tau}_d - \boldsymbol{\tau}), \tag{32}$$

in which $\boldsymbol{K}_P = k_P\boldsymbol{I}_{m\times m}$ stands for the proportional controller gain matrix for the inner loop, m represents the number of actuators, and $\boldsymbol{I}$ indicates the unity matrix. Next, consider

$$\boldsymbol{\tau}_d = \bar{\boldsymbol{\tau}}_d + \alpha\mathbf{Q}, \tag{33}$$

where

$$\bar{\boldsymbol{\tau}}_d = -\hat{\boldsymbol{J}}^{\dagger}\boldsymbol{F}_r. \tag{34}$$

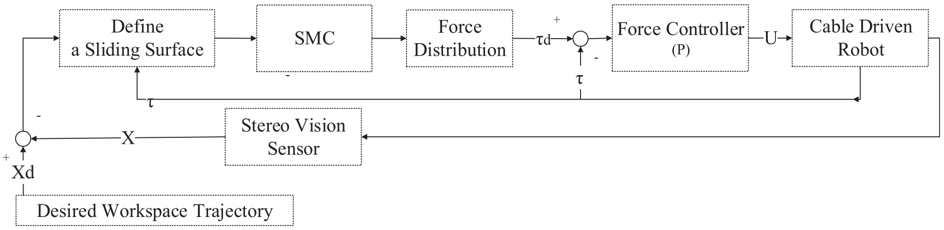

Fig. 4. Proposed control structure.

In the latter equation $\boldsymbol{Q}$ is the null space of the approximated Jacobian. Furthermore α is a scalar factor, which is selected so that the actuator forces remain in the feasible range $[\tau_{\min}, \tau_{\max}]$. Such a force distribution is necessary because of actuator redundancy, which results in a non-square Jacobian matrix. Therefore, redundancy resolution algorithms must be used to solve this problem. In the above equation, $\boldsymbol{F}_r$ can be determined as

$$\boldsymbol{F}_r = \hat{\boldsymbol{M}}\ddot{\mathbf{x}}_r + \hat{\boldsymbol{C}}\dot{\mathbf{x}}_r + \hat{\boldsymbol{G}} - \boldsymbol{K}_r\boldsymbol{s}_r, \tag{35}$$

in which $\boldsymbol{K}_r$ is a positive definite matrix.

5.1. Stability analysis

To analyze the stability of the proposed control laws, consider the following Lyapunov function candidate:

$$V_r(t) = \frac{1}{2}\boldsymbol{s}_r^T(\boldsymbol{M}_T + \boldsymbol{K}_{pn}\boldsymbol{M})\boldsymbol{s}_r, \tag{36}$$

where $\boldsymbol{K}_{pn} = k_p\boldsymbol{I}_{n\times n}$, and where n denotes the degree of freedom. We differentiate $V(t)$ with respect to time,

$$\dot{V}_r(t) = \boldsymbol{s}_r^T(\boldsymbol{M}_T + \boldsymbol{K}_{pn}\boldsymbol{M})\dot{\boldsymbol{s}}_r + \boldsymbol{s}_r^T(\boldsymbol{C}_T + \boldsymbol{K}_{pn}\boldsymbol{C})\boldsymbol{s}_r. \tag{37}$$

To simplify, we find the equivalent of $(\boldsymbol{M}_T + \boldsymbol{K}_{pn}\boldsymbol{M})\dot{\boldsymbol{s}}_r$ as

$$(\boldsymbol{M}_T + \boldsymbol{K}_{pn}\boldsymbol{M})\dot{\boldsymbol{s}}_r = -\boldsymbol{C}_T\boldsymbol{s}_r - (\boldsymbol{M}_T\ddot{\mathbf{x}}_r + \boldsymbol{C}\dot{\mathbf{x}}_r + \boldsymbol{G}) + \boldsymbol{J}^T\boldsymbol{u}. \tag{38}$$

According to Eq. (32), we have

$$\begin{aligned} \boldsymbol{J}^T\boldsymbol{u} = & -\boldsymbol{J}^T\boldsymbol{K}_P(\boldsymbol{\tau}_d - \boldsymbol{\tau}) \\ = & \ \boldsymbol{J}^T\boldsymbol{K}_P\hat{\boldsymbol{J}}^\dagger\left(\hat{\boldsymbol{M}}\ddot{\mathbf{x}}_r + \hat{\boldsymbol{C}}\dot{\mathbf{x}}_r + \hat{\boldsymbol{G}} - \boldsymbol{K}_r\boldsymbol{s}_r\right) + \alpha\boldsymbol{J}^T\boldsymbol{K}_P\boldsymbol{Q} - \boldsymbol{K}_{pn}(\boldsymbol{M}\ddot{\mathbf{x}} + \boldsymbol{C}\dot{\mathbf{x}} + \boldsymbol{G}) \\ = & -\boldsymbol{K}_{pn}(\boldsymbol{M}\dot{\boldsymbol{s}}_r + \boldsymbol{C}\boldsymbol{s}_r + \boldsymbol{K}_r\boldsymbol{s}_r) + \left(\boldsymbol{J}^T\boldsymbol{K}_p\hat{\boldsymbol{J}}^\dagger - \boldsymbol{K}_{pn}\right)\boldsymbol{F}_r - \alpha\tilde{\boldsymbol{J}}^T\boldsymbol{K}_p\boldsymbol{Q} + \boldsymbol{K}_{pn}\left(\tilde{\boldsymbol{M}}\ddot{\mathbf{x}}_r + \tilde{\boldsymbol{C}}\dot{\mathbf{x}}_r + \tilde{\boldsymbol{G}}\right). \end{aligned} \tag{39}$$

Pursuant to Eq. (38), one may reach to

$$\begin{aligned} (\boldsymbol{M}_T + \boldsymbol{K}_{pn}\boldsymbol{M})\dot{\boldsymbol{s}}_r = & -\boldsymbol{K}_{pn}\boldsymbol{C}\boldsymbol{s}_r - \boldsymbol{K}_{pn}\boldsymbol{K}_r\boldsymbol{s}_r - \boldsymbol{C}_T\boldsymbol{s}_r - (\boldsymbol{M}_T\ddot{\mathbf{x}}_r + \boldsymbol{C}\dot{\mathbf{x}}_r + \boldsymbol{G}) \\ & + \left(\boldsymbol{J}^T\boldsymbol{K}_p\hat{\boldsymbol{J}}^\dagger - \boldsymbol{K}_{pn}\right)\boldsymbol{F}_r - \alpha\tilde{\boldsymbol{J}}^T\boldsymbol{K}_p\boldsymbol{Q} + \boldsymbol{K}_{pn}\left(\tilde{\boldsymbol{M}}\ddot{\mathbf{x}}_r + \tilde{\boldsymbol{C}}\dot{\mathbf{x}}_r + \tilde{\boldsymbol{G}}\right). \end{aligned} \tag{40}$$

We substitute the above results in Eq. (37) to get

$$\dot{V}_r(t) = \boldsymbol{s}_r^T(-\boldsymbol{K}_{pn}\boldsymbol{K}_r\boldsymbol{s}_r + \boldsymbol{K}_{pn}\rho_r), \tag{41}$$

in which ρ_r may be defined as

$$\rho_r = \left(\boldsymbol{J}^T\hat{\boldsymbol{J}}^\dagger - \boldsymbol{I}\right)\boldsymbol{F}_r - \alpha\tilde{\boldsymbol{J}}^T\boldsymbol{Q} + \left(\tilde{\boldsymbol{M}}\ddot{\mathbf{x}}_r + \tilde{\boldsymbol{C}}\dot{\mathbf{x}}_r + \tilde{\boldsymbol{G}}\right) - \boldsymbol{K}_{pn}^{-1}(\boldsymbol{M}_T\ddot{\mathbf{x}}_r + \boldsymbol{C}\dot{\mathbf{x}}_r + \boldsymbol{G}). \tag{42}$$

It can be inferred from the above equation that by increasing the controller gain k_p, the effect of uncertainty in dynamic parameters like $\boldsymbol{M}_T, \boldsymbol{C}_T$, and $\boldsymbol{G}_T$ is significantly reduced. Furthermore, assuming $|\rho_r| < \boldsymbol{a}_0 + \boldsymbol{a}_1|\boldsymbol{s}_r|$, in which $\boldsymbol{a}_0$ is a positive vector and $\boldsymbol{a}_1$ is a diagonal matrix with positive elements, we have

$$\dot{V}_r(t) < \boldsymbol{s}_r^T(-\boldsymbol{K}_{pn}\boldsymbol{K}_r\boldsymbol{s}_r + \boldsymbol{K}_{pn}\boldsymbol{a}_0 + \boldsymbol{K}_{pn}\boldsymbol{a}_1|\boldsymbol{s}_r|). \tag{43}$$

We simplify to find

$$\dot{V}_r(t) < \boldsymbol{K}_{pn}(-\boldsymbol{K}_r + \boldsymbol{a}_1)\|\boldsymbol{s}_r\|^2 + \boldsymbol{K}_{pn}\boldsymbol{a}_0\|\boldsymbol{s}_r\|. \tag{44}$$

The above relation proves the UUB stability of $\boldsymbol{s}_r$. Therefore, it can be assumed that $\boldsymbol{s}_r$ is bounded from above by $\boldsymbol{s}_r < \bar{\boldsymbol{s}}_r$. This result will be used for the stability analysis in the next section.

Now, in order to show the stability of $\boldsymbol{s}_x$, we must determine an upper bound for $\dot{\boldsymbol{s}}_r$. To this end, and according to Eq. (40), we have

$$\dot{\boldsymbol{s}}_r = -(\boldsymbol{M}_T + \boldsymbol{K}_{pn}\boldsymbol{M})^{-1}(\boldsymbol{K}_{pn}\boldsymbol{C}\boldsymbol{s}_r - \boldsymbol{K}_{pn}\boldsymbol{K}_r\boldsymbol{s}_r - \boldsymbol{C}_T\boldsymbol{s}_r + \boldsymbol{K}_{pn}\rho). \tag{45}$$

Considering $\boldsymbol{s}_r$ being bounded, an upper bound for $\dot{\boldsymbol{s}}_r$ may be defined as

$$|\dot{\boldsymbol{s}}_r| < \lambda_{\max}\left((\boldsymbol{M}_T + \boldsymbol{K}_{pn}\boldsymbol{M})^{-1}\right)(\lambda_{\max}(\boldsymbol{K}_{pn}\zeta_c + \zeta_{c_T})\bar{\boldsymbol{s}}_r + \lambda_{\max}(\boldsymbol{K}_{pn}\boldsymbol{K}_r)\bar{\boldsymbol{s}}_r\boldsymbol{K}_{pn}\boldsymbol{a}_0 + \lambda_{\max}(\boldsymbol{K}_{pn}\boldsymbol{a}_1)\bar{\boldsymbol{s}}_r). \tag{46}$$

In the next section, we will use the upper bound obtained for $\dot{\boldsymbol{s}}_r$ to analyze the stability of $\boldsymbol{s}_x$.

5.2. Stability of $\boldsymbol{s}_x$

Consider the following Lyapunov function candidate:

$$V_x(t) = \frac{1}{2}\boldsymbol{s}_x^T(\boldsymbol{I} + \gamma\boldsymbol{M})\boldsymbol{s}_x. \tag{47}$$

Differentiate $V_x(t)$ with respect to time,

$$\dot{V}_x(t) = \boldsymbol{s}_x^T(\boldsymbol{I} + \gamma\boldsymbol{M})\dot{\boldsymbol{s}}_x + \frac{1}{2}\boldsymbol{s}_x^T\left(\gamma\dot{\boldsymbol{M}}\right)\boldsymbol{s}_x. \tag{48}$$

Consider Eq. (29) and the above equation as

$$\dot{V}_x(t) = \boldsymbol{s}_x^T(\boldsymbol{I} + \gamma\boldsymbol{M})\dot{\boldsymbol{s}}_x + \boldsymbol{s}_x^T(\gamma\boldsymbol{C})\boldsymbol{s}_x. \tag{49}$$

To simplify the above equation, we must find $(\boldsymbol{I} + \gamma\boldsymbol{M})\dot{\boldsymbol{s}}_x$. Since

$$\begin{aligned}\dot{\boldsymbol{s}}_x = &\ \dot{\boldsymbol{s}}_r - \gamma\dot{\sigma}\\ = &\ \dot{\boldsymbol{s}}_r - \gamma(\boldsymbol{M}\dot{\boldsymbol{s}}_x + \boldsymbol{C}\dot{\boldsymbol{s}}_x + \boldsymbol{K}_I sgn(\boldsymbol{s}_x) + \rho_x),\end{aligned} \tag{50}$$

we may write

$$(\boldsymbol{I} + \gamma\boldsymbol{M})\dot{\boldsymbol{s}}_x = \dot{\boldsymbol{s}}_r - \gamma\boldsymbol{C}\boldsymbol{s}_x - \boldsymbol{K}_I sgn(\boldsymbol{s}_x) + \rho_x. \tag{51}$$

We substitute the above equation in (49) to find

$$\begin{aligned}\dot{V}(t) = &\ \boldsymbol{s}_x^T(\dot{\boldsymbol{s}}_r - \gamma\boldsymbol{C}\boldsymbol{s}_x - \boldsymbol{K}_I\gamma sgn(\boldsymbol{s}_x)) + \boldsymbol{s}_x^T\boldsymbol{C}\gamma\boldsymbol{s}_x\\ = &\ \boldsymbol{s}_x^T(\dot{\boldsymbol{s}}_r - \boldsymbol{K}_I\gamma sgn(\boldsymbol{s}_x) + \rho_x).\end{aligned} \tag{52}$$

According to the boundedness properties obtained in the previous section, by selecting a sufficiently large gain $\boldsymbol{K}_I$, one may produce a negative value for the derivative of the Lyapunov function, and thereby guarantee the closed-loop stability of the overall system.

5.3. Force inner loop characteristics

In the previous section, we showed that using a force sensor in the inner loop controller is highly beneficial for reducing the effect of uncertainty on the robot tracking performance. In this section, we will examine this effect in the following cases.

- By selecting a high-gain inner loop controller, the actuator dynamics might be significantly reduced. Thus, in this situation, the structural dynamics are considered to be the dominant dynamics. When the structural dynamics are simple and well known, the inner loop force controller is very beneficial to the overall tracking performance.
- In the presence of high measurement noise, not possible to freely increase the gains of the inner loop controller. Under such conditions, it is not very beneficial to apply an inner loop force controller. As can be seen from Eq. (42), when $\boldsymbol{K}_p$ is too small, it not only fails to eliminate the destructive effect of the actuator dynamics, but might also increase the uncertainty profile.
- In the case of using a gearbox to increase actuator torque, actuator dynamics are dominant, and so the inner loop force controller is very effective. On the other hand, when the power transmission system is directly derived, structural dynamics are dominant and the proposed force controller will not be as effective as it would be in geared actuators.
- For the purpose of designing an integral controller for cable forces, we introduce a new sliding surface called $\boldsymbol{s}_r$. By applying such an algorithm alongside the proportional force controller, one may greatly improve the tacking efficiency. However, selecting inappropriate gains for this structure may lead to improper position tracking. In other words, there is a trade-off between position tracking and cable force regulation.

6. Experimental setup

In this section, we verify the proposed controller's effectiveness by implementing it on an ARAS-CAM suspended cable-driven robot. ARAS-CAM is a deployable cable-driven robot. Table 1 gives its technical specifications. The ARAS research group built this robot for applications that require a deployable robot with a large workspace, such as video-capturing and building 3D printers. The structure of the current version of ARAS-CAM is fixed and is not reconfigurable. However, in the next versions of the robot, the mechanical structure will be modified such that quick transferring and installation would be feasible. This in turn, can provide the opportunity to extend the ARAS-CAM applications in scenarios where long term operation of the robot is not an objective. For example, in the application of using the robot for the movie industry, the movability of the robot from one filming site to another would be important. Now, owing to its easy calibration and control procedure, the Deployable ARAS CAM can address this very problem.

Table 1
Kinematic and dynamic parameters of ARAS-CAM.

Parameter	unit	value
End-effector mass	kg	1 or 4.5
End-effector inertia	kg m^2	$\simeq 0$
Gear ratio	Direct drive	1
Gravity acceleration	m/s^2	9.8
Drum radius	cm	3.5
Number of pulleys	–	4
Parameter a in Fig. 2	m	3.56
Parameter b in Fig. 2	m	7.05
Parameter h in Fig. 2	m	4.23

ARAS-CAM has four actuators covering a workspace of $6^m \times 8^m \times 4^m$ and 3 controlled degrees of freedom. Hence, the robot is redundantly actuated and can ameliorate the force distribution in the cables in an enlarged workspace. The robot implementation procedure is accomplished without using any complex or expensive measuring instruments. Because the robot is deployable, there is up to a 5% dimension uncertainty in ARAS-CAM's kinematic structure. In terms of measurement systems, ARAS-CAM is equipped with three types of sensors, including motor encoders, force sensors, and a stereo camera capable of providing accurate position measurements for the end-effector. The subsections below provide a brief representation of the designed system.

6.1. Cable length measurement system

We created a special design for the cable winches such that the drum moves along its axis with a pitch equal to the cable width. This prevents cable cluttering. Fig. 1 shows this mechanism. By employing this method of cable control, the cable lengths can be accurately inferred from encoder outputs. Because the encoders used in this robot are not absolute, measuring the cable lengths requires us to first determine the cables' initial lengths. This is achieved by equipments like a cheap laser length measurer. It should be noted that the laser sensor is only used for measuring the initial cable lengths for the calibration procedure. In this step, the end-effector position is set to a given home point and the robot has no movement.

6.2. Force sensors

To measure cable tension, we designed a load cell sensor that is placed in a structure of three pulleys, as shown in Fig. 5. Previous versions of this force-sensing mechanism are detailed in [17], in which low weight force sensors are attached to the

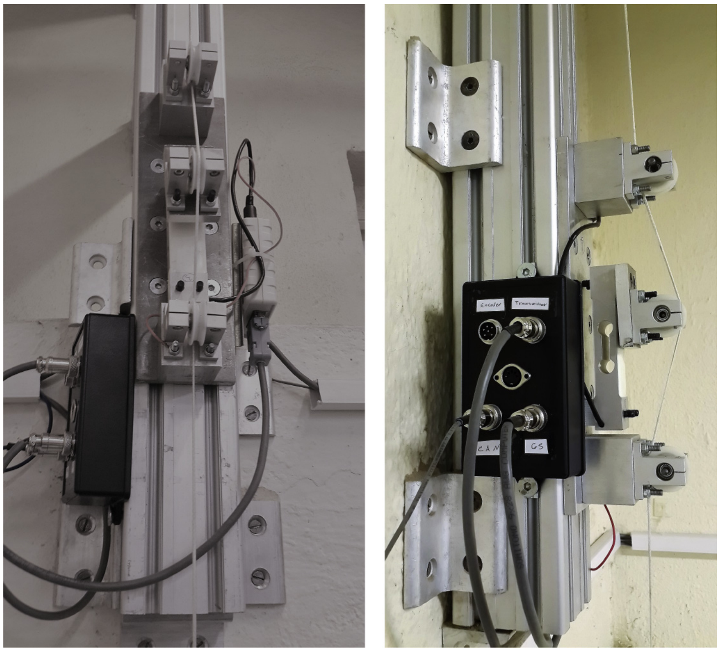

Fig. 5. System designed to measure cable force in a fixed location.

cable near the end-effector. One major drawback of such a design is that weights of the sensors diverts the cable model from a model for an ideal straight and weightless cable. Moreover, the wires from the sensors overhang and create operational problems. However, the proposed force measurement system in this paper is designed such that the load cell sensors do not impose any weight on the cables, and therefore, both wiring and sagging problems are avoided.

6.3. Vision sensor

The third sensor in our robot is a stereo camera. It has a resolution of 640 × 480 pixels, and is capable of capturing data at a rate of 100 Hertz. We constructed an extremely low-cost IR tracking system by attaching an infrared LED to the end-effector and placing visible-light filters in front of the cameras. After capturing the images, we used the software we developed in order to perform a simple thresholding operation: two pairs of pixel coordinates corresponding to the image coming from each camera are extracted and undistorted, and finally used for calculating the 3D world coordinate of the LED. Fig. 6 shows the infrared LED attached to the robot end-effector, and Fig. 6(a) shows the designed stereo vision set. By placing physical light filters in front of the cameras, and performing the stereo image processing for just two individual extracted pixels at each measurement step, we significantly reduced the computational load. Thus, we achieved real-time measurements with relatively low-cost processors.

6.4. Real-time control system

Fig. 7 shows a block diagram of the control system. The host computer serves as the user interface and enables the user to edit and modify the control structure and parameters. The target computer is a real-time processing unit on which the Simulink Real-time Target is installed. For the IO's, we used a number of PCI input/output DAQ boards and developed the necessary custom drivers for them to work within the Simulink real-time target framework.

6.5. Force redundancy resolution

The force distribution problem is one of the most challenging issues in cable-driven redundant robots. In this paper, the redundancy resolution is addressed in the Eqs. (33) and (34).

According to the fact that the robot has a redundant in actuator, its Jacobian matrix is not square and invertible. In the other words, there are infinite combinations of cable tension that produce the same desired Cartesian force $\boldsymbol{F}_r$. Now, all of these solutions can be achieved through changing the α parameter in Eq. (33). It is important to note that during the robot's maneuver, all the cables must stay tensioned thus, all cable forces must be positive. In order to achieve this, the value of α in Eq. (33) should be selected carefully. Since the task of choosing a proper α value is a challenging one, a large number of studies has been carried out and published [25–27]. In all of these works, it is assumed that the robot is kept in its feasible workspace. However, in this paper, without direct computation of α, a new fast algorithm applicable in real-time applications is proposed. This method is based on the control allocation theory which is investigated in [28–30]. The procedure of the proposed method is shown in Table 2. As represented in this table, the initial cable forces are determined by the Eq. (34). If one of the cable forces obtained by Eq. (34) has a value less than $\tau_{\min}$,

$$\tau_{d_i} < \tau_{\min}, \quad i = 1, \ldots, 4 \tag{53}$$

the force of this cable should be assigned to $\tau_{\min}$. To determine the other cable forces, the column of the Jacobian matrix corresponding to this cable, i^{th} column, is multiplied by $\tau_{\min}$ to produce the Cartesian force $\boldsymbol{F}_r$. Next, the residual Cartesian force, $\boldsymbol{F}''_r = \boldsymbol{F}_r - \boldsymbol{F}'_r$, would be distributed on the other cables except the ith one. Distribution of $\boldsymbol{F}''_r$ on these cables is done through a square matrix called $\boldsymbol{J}''_r$ which is obtained by removing the $i^{t}h$ column of the Jacobian matrix. Computing the inverse of $\boldsymbol{F}''_r$ and using

$$\boldsymbol{\tau}'_d = \boldsymbol{J}_r''^{-1} \boldsymbol{F}''_r, \tag{54}$$

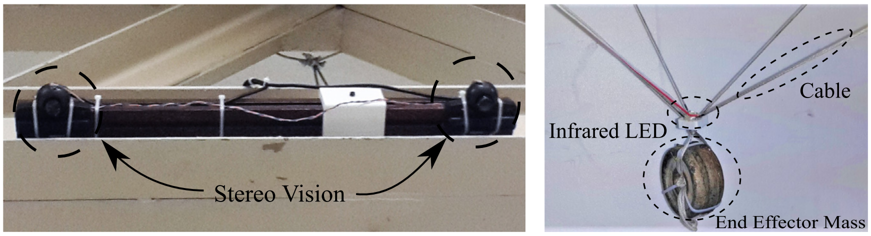

Fig. 6. Prototype of a stereo vision system.

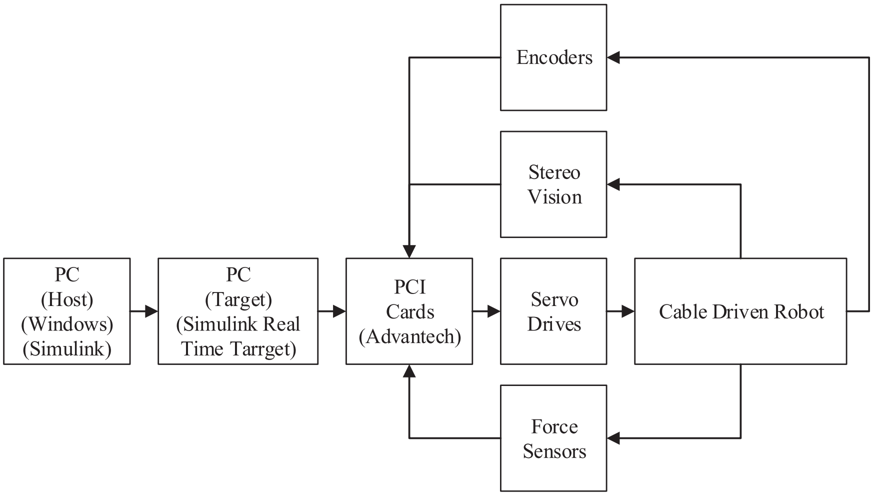

Fig. 7. Real-time control system.

Table 2
Redundancy resolution algorithm.

```
Input: $(\boldsymbol{J}_r, \boldsymbol{F}_r)$
Output: $\boldsymbol{\tau}_d$
$\bar{\boldsymbol{\tau}}_d \leftarrow -\hat{\boldsymbol{J}}^{\dagger}\boldsymbol{F}_r$
$\bar{\boldsymbol{\tau}}_d = \left[\tau_{d_1}, \ldots, \tau_{d_i}, \ldots, \tau_{d_4}\right]^T \qquad i = 1, \ldots, 4$
$\hat{\boldsymbol{J}}^T = \left[\widehat{J}_1, \ldots, \widehat{J}_i, \ldots, \widehat{J}_4\right]_{3\times4} \qquad i = 1, \ldots, 4$
if $\bar{\boldsymbol{\tau}}_{d_i} < \tau_{\min}$
  $\boldsymbol{F}'_r = \widehat{J}_i \tau_{\min}$
  $\boldsymbol{F}''_r = \boldsymbol{F}_r - \boldsymbol{F}'_r$
  $\boldsymbol{J}''_r = \widehat{J}^T$ without $\widehat{J}_i$
  $\boldsymbol{\tau}'_d = \mathrm{inv}(\boldsymbol{J}''_r)\boldsymbol{F}''_r$
  if $\tau'_{d_i} < \tau_{\min}$
    Robot is not in its feasible workspace
  else
    $\boldsymbol{\tau}_d \leftarrow (\boldsymbol{\tau}'_d, \tau_{\min})$
  end if
else
$\boldsymbol{\tau}_d \leftarrow \bar{\boldsymbol{\tau}}_d$
end if
```

the other cable forces can be calculated. It can be shown that $\boldsymbol{F}_r$ would not be applicable if one of these computed cable forces is less than $\tau_{\min}$. In other words, the desired acceleration is out of the feasible workspace. Therefore in this case, redesigning the end-effector trajectory would be necessary.

7. Experimental results

In this section, we examine the tracking performance of a circular trajectory of the closed-loop system by implementing the proposed cascade controller. It is worth mentioning that in the experiments, the controller gains are set in such a way that the stability of the system in the presence of model uncertainty is guaranteed. Table 3 presents all the parameter values in the real-time controller proposed in Eqs. (24), (32) and (35). Furthermore, We conducted two experiments to investigate the inner force controller in various robots with different dynamic characteristics. The first experiment uses a light 1 kg payload. As expected, we observed that employing an inner force control loop here improved performance. In fact in this case, where actuator dynamics are dominant, the application of an inner force controller greatly reduced the effects of nonlinearities and resulted in better performance.

Fig. 8 illustrates the desired trajectory and the closed-loop tracking performance using the cascade control law. The tracking error is depicted in Fig. 9. As seen in these figures, the tracking errors are in the order of millimeters in all three direc-

Table 3
The proposed controller parameters.

K_p	γ	K_I	Λ	K_r
2	0.0005	10	0.1	100

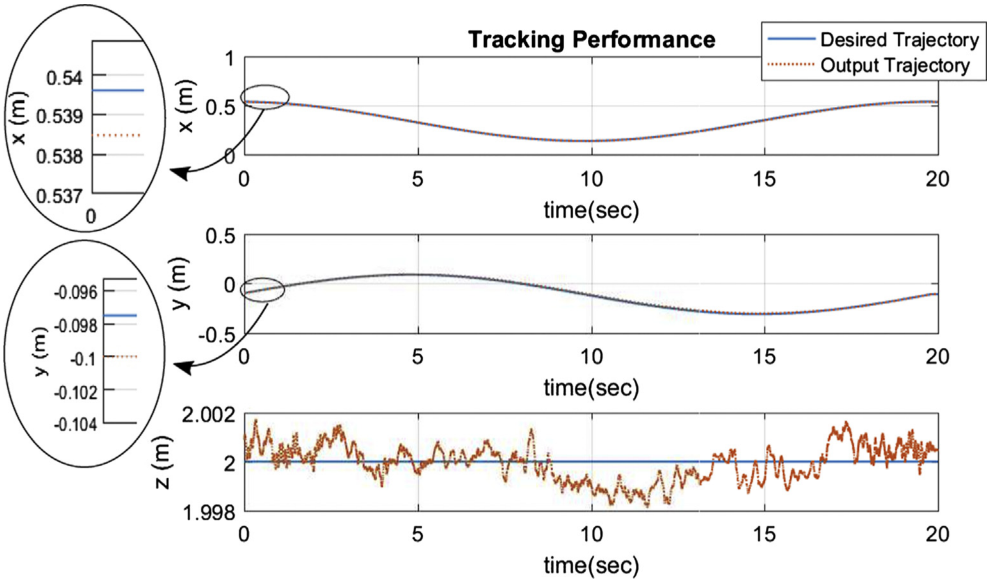

Fig. 8. Performance of tracking a desired trajectory when end-effector mass is 1 kg.

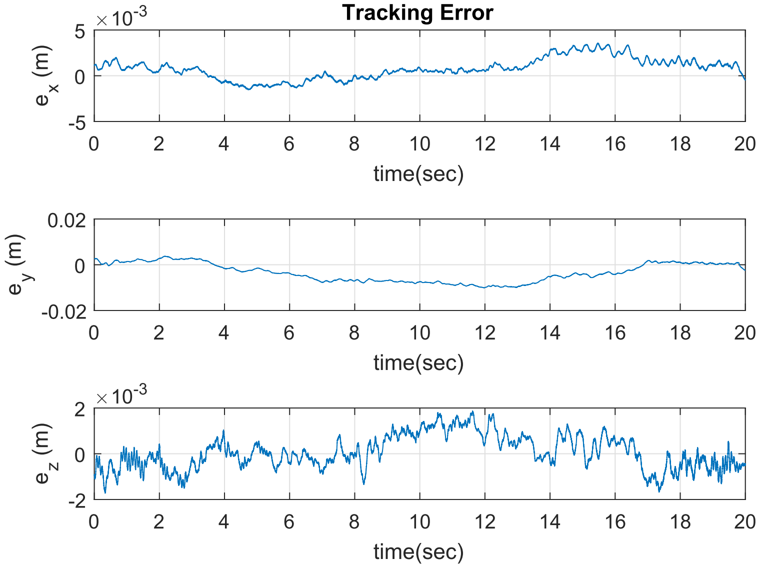

Fig. 9. Tracking error of a desired trajectory when end-effector mass is 1 kg.

tions. As shown in Fig. 9, the structural geometry of the robot is a cuboid with the dimensions of 4.56 × 7.05 m^2. Therefore, the difference in the x and y response is expected. On the other hand, the four actuators used in the ARAS-CAM are not completely identical and do not perform similarly. These reasons lead to a different results in the two x and y axes. Fig. 10 presents the cable lengths in this experiment. As can be seen, the cables vary in length by about 0.3 m. Moreover, the measured cable tension during a robot maneuver is shown in Fig. 11, which indicates that all the forces are positive and all the cables are under tension. Finally, Fig. 12 illustrates the desired circular trajectory alongside the robot tracking performance. This

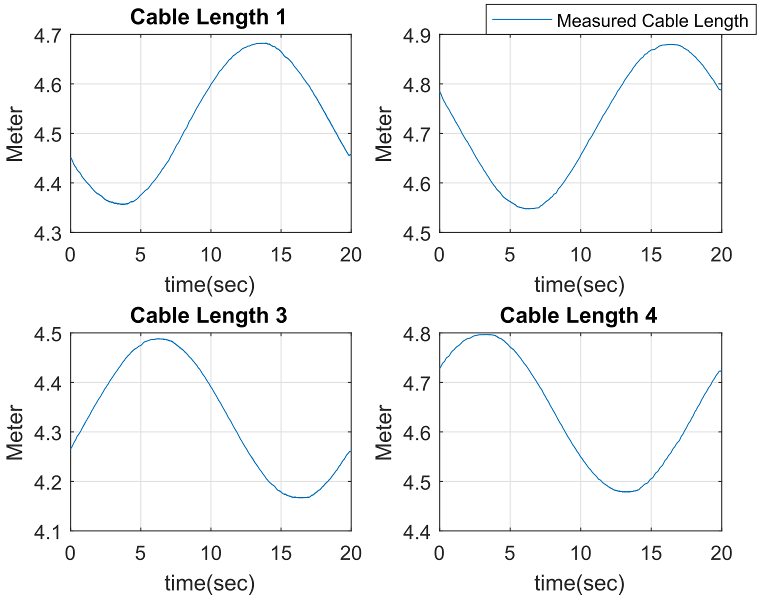

Fig. 10. Cable length variation in the experiment when end-effector mass is 1 kg.

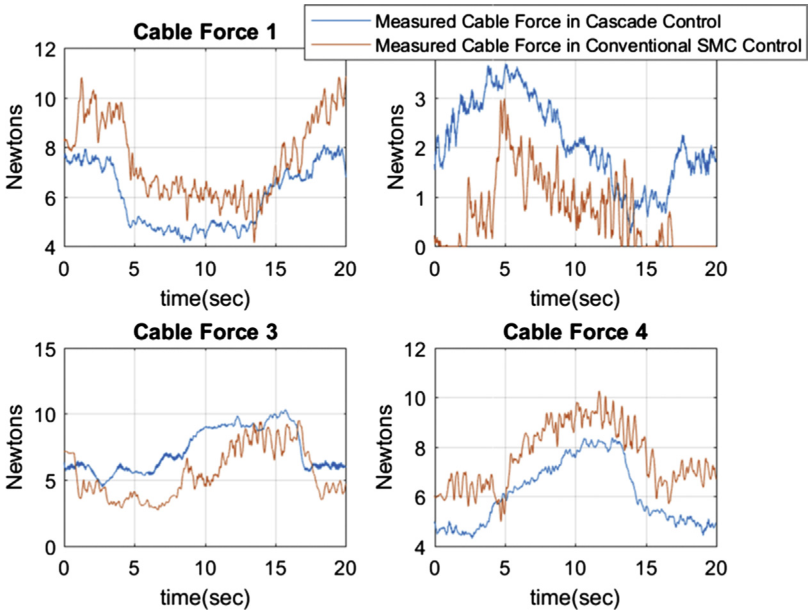

Fig. 11. Measured cable forces when end-effector mass is 1 kg.

figure also shows the tracking error for an SMC controller without any inner force controller in order to demonstrate the effectiveness of the proposed method. As can be seen, employing the cascade control law has significantly increased the tracking accuracy. This method is so effective because the inner-loop force controller handles complex nonlinearities such as friction and motor dead-zone present in a real power transmission system. Moreover, employment of inner-loop force controllers could lead to better performance in the case of implementing cable force distribution algorithms, which in turn would prevent cables to become loose. during robot maneuvers. As depicted in Fig. 11, during the circular maneuver of the robot, omitting the inner loop controller frequently caused the force applied by the second cable to become zero. In other words, the robot often lost one actuator. Consequently, the tracking performance was much worse.

In the second experiment, the payload mass increased to 4.5 kg. As a result, in this case structural dynamics are dominant; and as mentioned, an inner force controller is not expected to be very beneficial. This hypothesis is supported by

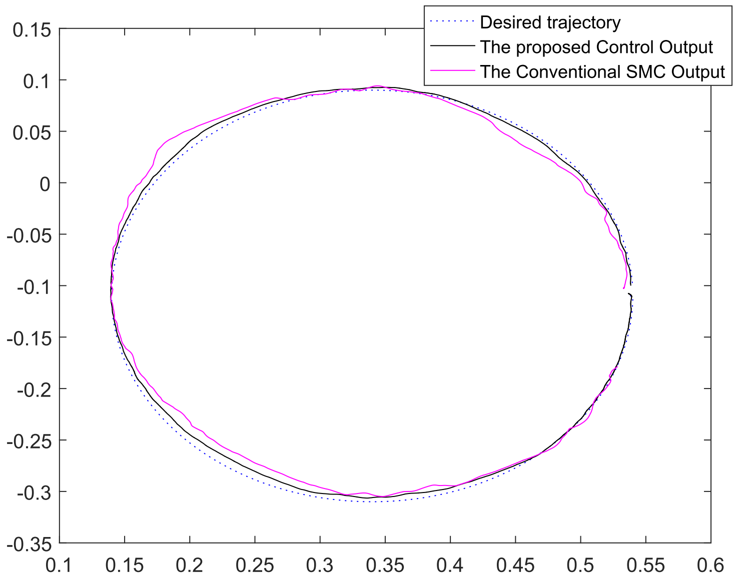

Fig. 12. Performance of tracking a desired trajectory in the x–y plane when end-effector mass is 1 kg.

Table 4
Comparison of robot performance.

	End-effector mass	K_p	γ	RMS error
First test	1 kg	0	0	0.0084
	1 kg	2	0.0005	0.0039
Second test	4.5 kg	0	0	0.0065
	4.5 kg	2	0.0005	0.0039

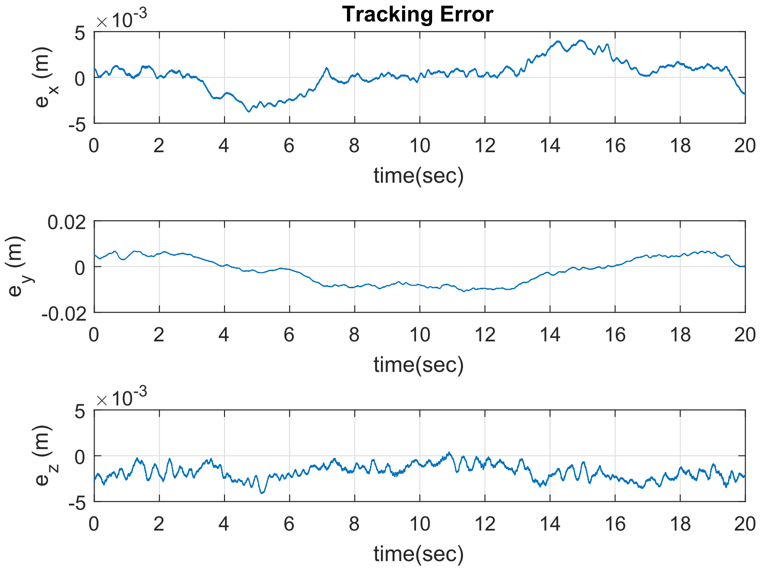

Fig. 13. Tracking error of a desired trajectory when end-effector mass is 4.5 kg.

the results in Table 4, which compares the results of these two tests in terms of RMS error. As can be seen, the use of an inner force loop in CDPMs is generally useful, although its advantages are more significant when the end-effector is relatively light and/or the actuators are gear-driven. As shown in Table 4, in the first test (where actuator dynamics are dominant), the RMS error after applying $K_p = 2$ and $\gamma = 0.0005$ is reduced by as much as 0.0045^{m}. By contrast, in the second test (where struc-

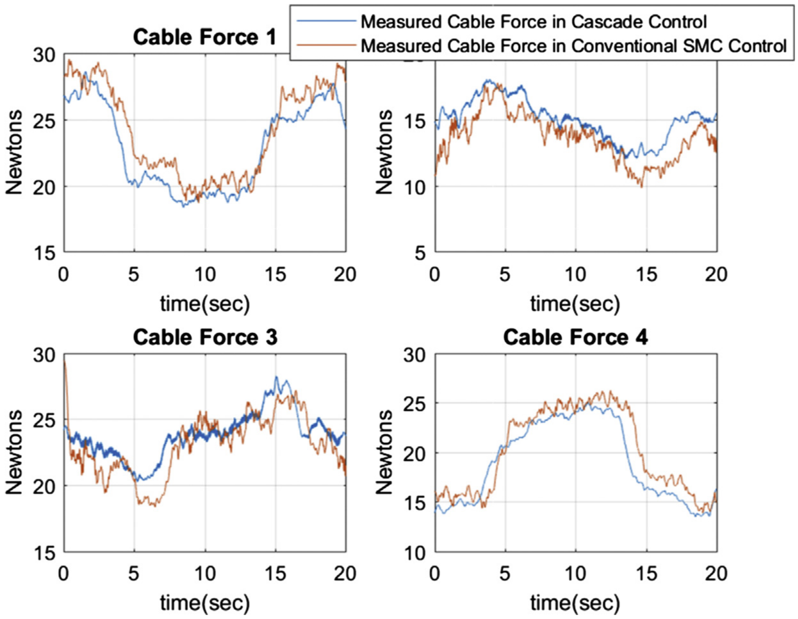

Fig. 14. Measured cable forces when end-effector mass is 4.5 kg.

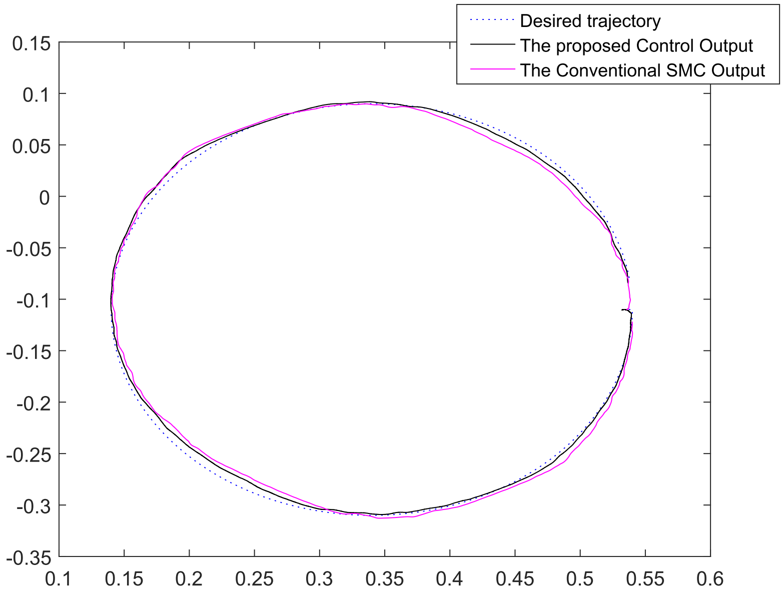

Fig. 15. Performance of tracking a desired trajectory in the x–y plane when end-effector mass is 4.5 kg.

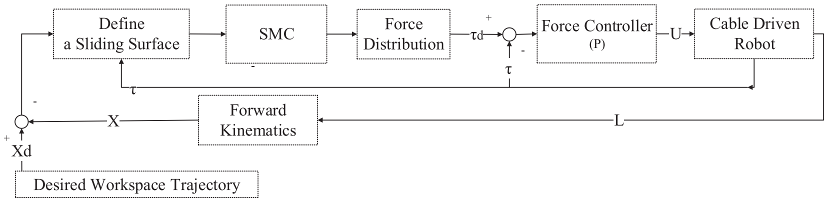
Define
a Sliding Surface
SMC
Force
Distribution
τd
+
-
τ
Force Controller
(P)
U
Cable Driven
Robot
-
τ
Forward
Kinematics
X
L
-
+
Xd
Desired Workspace Trajectory

Fig. 16. Implementation of the proposed algorithm without use of a vision sensor.

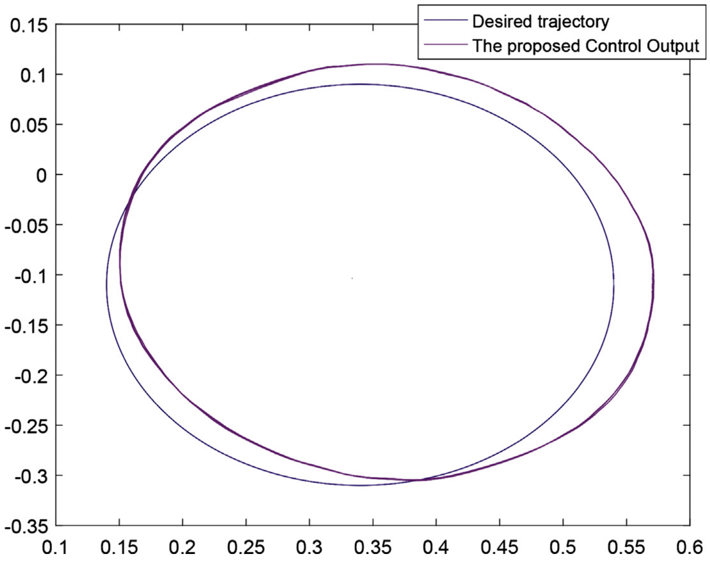

Fig. 17. Implementation results showing cable robot repeatability when a vision sensor is not used.

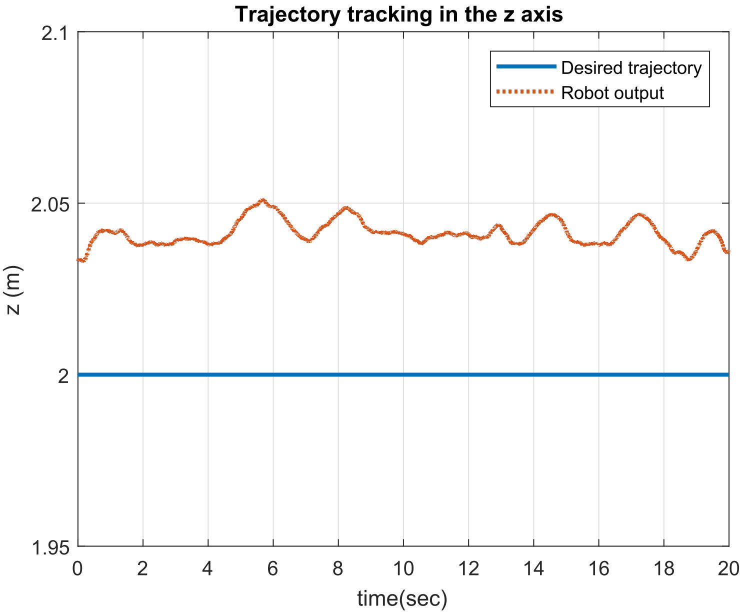

Fig. 18. Trajectory tracking in the *z* axis when a vision sensor is not used.

Table 5
Tracking errors in the third test.

RMS error	$\|e_x\|$	$\|e_y\|$	$\|e_z\|$
	0.0137	0.0146	0.025

tural dynamics are dominant), this reduction is just 0.0025^{m}. These results clearly show that in the case of actuator dynamics dominance, using the force controller is notably beneficial.

Figs. 13–15 illustrate the tracking error, the cable forces, and the desired circular trajectory in the horizontal plane and the closed loop tracking performance of the SMC controller with and without the force inner loop. As can be seen from these figures, the proposed controller has provided suitable tracking performance, while keeping all the cables under tension. Furthermore, we observe that the trajectory is more precisely tracked when the cascade control law is used.

In all the reported experiment results, the IR tracking device is employed as the robot positioning system in order to verify the final absolute position tracking of the system via different control laws. However, such a measurement system may not be feasible in a real outfield deployable robotic system (due to the required calibration process and limited field of measurement space). Therefore, two other practical alternatives may be considered. In the first alternative, a block diagram of which is shown in Fig. 16, the end-effector pose is obtained from a forward kinematics solution taking as inputs the cable-length measurements from the motor encoders. The main advantage of this alternative is that it uses sensors that are generally readily embedded in outdoor deployable robots. Its disadvantage is that due to the structural uncertainties of the system, a non-vanishing tracking error will be seen in the outcome performance. This drawback is unavoidable, so this alternative is best suited to applications where the absolute positioning is not vital, and robot repeatability is of greater importance.

The second alternative is to take advantage of simultaneous localization and mapping (SLAM) methods and visual odometry techniques to provide a position measurement for the controller. In this approach, the camera may be installed on the end-effector itself; consequently, workspace limitation is no longer an issue. No sophisticated calibration process is required, making this a suitable method for deployable robots. However, there are also drawbacks, such as intensive processing power demands and environment dependent measurement performance.

We chose to use the first alternative in this paper, since it is more economical and much faster compared to the intrinsic visionary delay. To evaluate the repeatability criteria—one of the most important performance measures in industrial robotic systems—we designed and implemented another experiment. In this experiment, the motor encoders and forward kinematic solution are used to provide position feedback, and the robot is commanded to follow a desired circular trajectory with a 0.2 m radius for four turns. As shown in Fig. 17, the robot's repeatability performance is quite acceptable and absolute positioning shows a non-vanishing errors in both directions. Fig. 18 also shows the robot performance in the z axis when the vision sensor is not used. The norm of these errors are separately shown in Table 5 for three cartesian axes. As it can be seen in Table 5 the error norms in all three axes are relatively large. This means that the path in which the robot end-effector moves is far from the desired trajectory, but as shown in Fig. 17, this path for all four turns is identical.

8. Conclusions

This paper aimed to expand the applications of cable-driven parallel robots. We considered the idea of a deployable design, and derived the kinematic and dynamic formulation of a cable-driven suspended robot. We showed that parameter uncertainties in deployable cable-driven robots can have a strong effect on the kinematic equations, especially the Jacobian matrix. We then showed that applying a cascade structure in CDPMs can greatly reduce the effects of uncertainty in the actuator dynamics. We proposed a robust cascade controller that would control the robot in the presence of such kinematic and dynamic uncertainties. Finally, we conducted three experiments to verify the stability criteria for such a controller. Results showed that our controller achieved a suitable tracking performance and met the repeatability criteria.

Acknowledgments

The authors would like to thank the Iranian National Science Foundation (INSF) for partially supporting this research under Grant No. **96001803**. The authors greatly appreciate Mr. Salman Kariminasab and Mr. Alireza Bourbour for their contribution to the experimental setup and for their time in discussing this work.

Conflict of interest

The authors declare that there is no conflict of interests regarding the publication of this article.

References

[1] T. Tjahjowidodo, K. Zhu, W. Dailey, E. Burdet, D. Campolo, Multi-source micro-friction identification for a class of cable-driven robots with passive backbone, in: Mechanical Systems and Signal Processing, Elsevier, 2016, pp. 152–165, vol. 80.

[2] B.L. Jordan, M.A. Batalin, W.J. Kaiser, Nims rd: a rapidly deployable cable based robot, in: Proceedings 2007 IEEE International Conference on Robotics and Automation, IEEE, 2007, pp. 144–150.

[3] P.H. Borgstrom, B.L. Jordan, B.J. Borgstrom, M.J. Stealey, G.S. Sukhatme, M.A. Batalin, W.J. Kaiser, Nims-pl: a cable-driven robot with self-calibration capabilities, IEEE Trans. Robot. 25 (5) (2009) 1005–1015.

[4] P. Bosscher, R.L. Williams, M. Tummino, A concept for rapidly deployable cable robot search and rescue systems, in: ASME 2005 International Design Engineering Technical Conferences and Computers and Information in Engineering Conference, 2005, pp. 589–598.

[5] J.P. Merlet, Marionet, a family of modular wire-driven parallel robots, Adv. Robot Kinematics: Motion Man Mach. (2010) 53–61.

[6] C.C. Cheah, S. Kawamura, S. Arimoto, Feedback Control For Robotic Manipulator With an Uncertain Jacobian Matrix, Adv. Robot Kinematics: Motion Man Machin J. Robot. Syst. 16 (2) (1999) 119–134.

[7] C.C. Cheah, S. Kawamura, S. Arimoto, K. Lee, H tuning for task-space feedback control of robot with uncertain jacobian matrix, Automatic Control IEEE Trans. 46 (8) (2001) 1313–1318.

[8] C.C. Cheah, M. Hirano, S. Kawamura, S. Arimoto, Approximate jacobian control for robots with uncertain kinematics and dynamics, Robot. Autom. IEEE Trans. 19 (4) (2003) 692–702.

[9] C.-C. Cheah, C. Liu, J.-J.E. Slotine, Adaptive jacobian tracking control of robots with uncertainties in kinematic, dynamic and actuator models, IEEE Trans. Autom. Control 51 (6) (2006) 1024–1029.

[10] C.C. Cheah, X. Li, Task-space Sensory Feedback Control of Robot Manipulators, Springer, 2015, vol. 73.

[11] G. Bartolini, A. Ferrara, A. Levant, E. Usai, On second order sliding mode controllers, in: Variable Structure Systems, Sliding Mode and Nonlinear Control, Springer, 1999, pp. 329–350.

[12] G. Bartolini, A. Pisano, E. Punta, E. Usai, A survey of applications of second-order sliding mode control to mechanical systems, Int. J. Control 76 (9–10) (2003) 875–892.

[13] V. Parra Vega, S. Arimoto, Y.H. Liu, G. Hirzinger, P. Akella, Dynamic sliding PID control for tracking of robot manipulators: theory and experiments, IEEE Trans. Robot. Autom. 19 (6) (2003) 967–976.

[14] M.A. Arteaga, A. Castillo-Sanchez, V. Parra-Vega, Cartesian control of robots without dynamic model and observer design, Automatica 42 (3) (2006) 473–480.

[15] A.J. Koshkouei, K.J. Burnham, A.S. Zinober, Dynamic sliding mode control design, IEE Proc.-Control Theory Appl. 152 (4) (2005) 392–396.

[16] M.S. Chen, C.H. Chen, F.-Y. Yang, An Ltr-observer-based dynamic sliding mode control for chattering reduction, Automatica 43 (6) (2007) 1111–1116.

[17] M.A. Khosravi, H.D. Taghirad, Robust PID control of fully-constrained cable driven parallel robots, Mechatronics 24 (2014) 87–97.

[18] A. Pott, H. Mütherich, W. Kraus, V. Schmidt, P. Miermeister, A. Verl, IPAnema: a family of cable-driven parallel robots for industrial applications, in: Cable-Driven Parallel Robots, Springer, 2013, pp. 119–134.

[19] R. Babaghasabha, M.A. Khosravi, H.D. Taghirad, Adaptive robust control of fully-constrained cable driven parallel robots, Mechatronics 25 (2015) 27–36.

[20] H. Taghirad, Parallel Robots Mechanics And Control, Taylor & Francis, CRC Press, 2013.

[21] R.J. Caverly, J.R. Forbes, Flexible cable-driven parallel manipulator control: maintaining positive cable tensions, IEEE Trans. Control Syst. Technol. 26 (5) (2018) 1874–1883.

[22] J. Begey, L. Cuvillon, M. Lesellier, M. Gouttefarde, J. Gangloff, Dynamic control of parallel robots driven by flexible cables and actuated by position-controlled winches, IEEE Trans. Robot. (2018).

[23] H. Jamshidifar, S. Khosravani, B. Fidan, A. Khajepour, Vibration decoupled modeling and robust control of redundant cable-driven parallel robots, IEEE/ASME Trans. Mechatron. 23 (2) (2018) 690–701.

[24] R. Babaghasabha, M.A. Khosravi, H.D. Taghirad, Adaptive robust control of fully constrained cable robots: singular perturbation approach, Nonlinear Dyn. (2016) 1–14.

[25] W. Kraus, Force Control of Cable–driven Parallel Robots, 2016.

[26] C. Gosselin, M. Grenier, On the determination of the force distribution in overconstrained cable–driven parallel mechanisms, Meccanica 46 (1) (2011) 3–15.

[27] H. Yuan, E. Courteille, D. Deblaise, Force distribution with pose–dependent force boundaries for redundantly actuated cable–driven parallel robots, J. Mech. Robot. 8 (4) (2016).

[28] A. Johansen, I. Fossen, Control allocation – a survey, Automatica 49 (5) (2013) 1087–1103.

[29] T. Bruckmann, A. Pott, Cable–driven Parallel Robots, Springer, 2012, vol. 12.

[30] R. Verhoeven, Analysis of the workspace of tendon based Stewart platforms (Ph. D. thesis), University of Duisburg-Essen, Germany, 2004.